RESEARCH ARTICLE

Key Points:
- Complex coseismic ground deformation can be explained by slip on six crustal fault segments
- Rupture process across multiple faults likely resulted from a triggering cascade between crustal faults
- Rupture speed was overall slow, but locally faster along individual fault segments

Supporting Information:
- Supporting Information S1
- Data Set S1
- Data Set S2
- Data Set S3

Correspondence to:
W. Xu, G. Feng, and L. Meng,
wenbin.xu@polyu.edu.hk;
fredgps@csu.edu.cn;
meng@epss.ucla.edu

Transpressional Rupture Cascade of the 2016 M_w 7.8 Kaikoura Earthquake, New Zealand

Wenbin Xu[1] [ID]**, Guangcai Feng[2], Lingsen Meng[3]** [ID]**, Ailin Zhang[3], Jean Paul Ampuero[4]** [ID]**, Roland Bürgmann[5]** [ID]**, and Lihua Fang[6]** [ID]

[1]Department of Land Surveying and Geo-informatics, Hong Kong Polytechnic University, Hong Kong, China, [2]School of Geosciences and Info-Physics, Central South University, Changsha, China, [3]Department of Earth Planetary and Space Sciences, University of California, Los Angeles, CA, USA, [4]Seismological Laboratory, California Institute of Technology, Pasadena, CA, USA, [5]Department of Earth and Planetary Science, University of California, Berkeley, CA, USA, [6]Institute of Geophysics, China Earthquake Administration, Beijing, China

Abstract Large earthquakes often do not occur on a simple planar fault but involve rupture of multiple geometrically complex faults. The 2016 M_w 7.8 Kaikoura earthquake, New Zealand, involved the rupture of at least 21 faults, propagating from southwest to northeast for about 180 km. Here we combine space geodesy and seismology techniques to study subsurface fault geometry, slip distribution, and the kinematics of the rupture. Our finite-fault slip model indicates that the fault motion changes from predominantly right-lateral slip near the epicenter to transpressional slip in the northeast with a maximum coseismic surface displacement of about 10 m near the intersection between the Kekerengu and Papatea faults. Teleseismic back projection imaging shows that rupture speed was overall slow (1.4 km/s) but faster on individual fault segments (approximately 2 km/s) and that the conjugate, oblique-reverse, north striking faults released the largest high-frequency energy. We show that the linking Conway-Charwell faults aided in propagation of rupture across the step over from the Humps fault zone to the Hope fault. Fault slip cascaded along the Jordan Thrust, Kekerengu, and Needles faults, causing stress perturbations that activated two major conjugate faults, the Hundalee and Papatea faults. Our results shed important light on the study of earthquakes and seismic hazard evaluation in geometrically complex fault systems.

1. Introduction

On 14 November 2016, an earthquake with moment magnitude (M_w) 7.8 took place in the Kaikoura region in the Marlborough fault system (MFS), South Island, New Zealand (Figure 1) (Hamling et al., 2017; Kaiser et al., 2017). The region straddles a wide zone of active crustal deformation associated with the oblique collision between the Pacific and Australian tectonic plates (Van Dissen & Yeats, 1991). The seismic moment tensor solutions for the Kaikoura earthquake indicate an oblique-reverse focal mechanism. The hypocenter of the earthquake was located at about 15 km depth near the town of Culverden (Kaiser et al., 2017). Long-period seismological analysis of the earthquake indicates that the event initiated as a small strike-slip rupture during the first 60 s followed by a major 20 s burst of moment release, resulting in a long rupture duration (Duputel & Rivera, 2017). More than 2,000 aftershocks occurred within three days, four of which had $M_w > 6$ (Figure 1). A large number of shallow aftershocks occurred across a broad area north of Canterbury (Kaiser et al., 2017).

Field investigations carried out by the Institute of Geological and Nuclear Sciences suggested that at least 14 major faults and seven minor faults including 11 previously unmapped faults ruptured from the Humps fault zone in the south to Cape Campbell ending offshore on the Needles fault (Figure 1) (Litchfield et al., 2016). The total length of the ruptured faults exceeds 150 km making it the largest historic event in the region. Field observations found that the largest surface fault offsets occurred along the Kekerengu fault with right-lateral slip reaching a maximum of about 11 m (Litchfield et al., 2016). Vertical displacements (6–8 m) were observed on the previously unmapped Papatea fault with a conjugate geometry to the Kekerengu fault (Litchfield et al., 2016). Continuous and campaign Global Positioning System (GPS) stations captured the coseismic ground deformation (Hamling et al., 2017). Stations near the epicenter show that the ground displacements were dominated by horizontal motions.

Multiple studies have been carried out to understand the complex faulting along the 2016 Kaikoura rupture using different data sets and methods (e.g., field observations, geodesy, seismology, satellite optical and
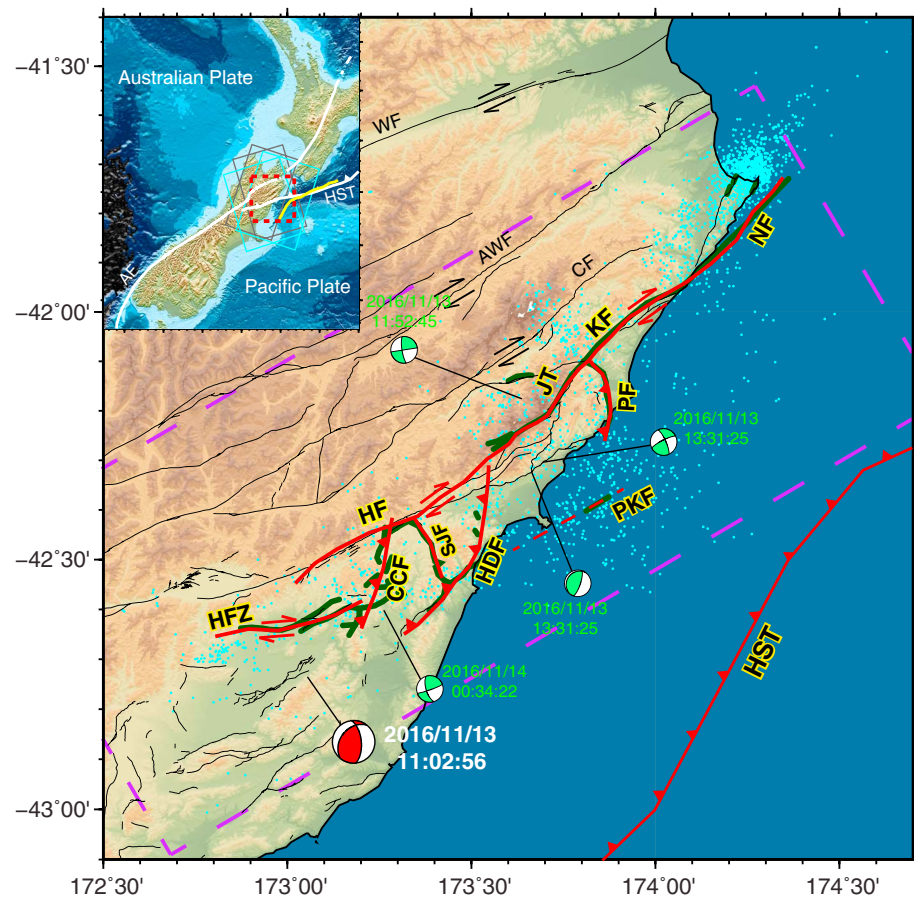
Figure 1. The regional setting and location of the 2016 Kaikoura earthquake in the northern South Island, New Zealand. The red lines show the location of the modeled faults. The dark green lines show the fault ruptures mapped. The mapped major faults are shown in black. AF, Alpine fault; WF, Wairau fault; AWF, Awatere fault; CF, Clarence fault; NF, Needles fault; KF, Kekerengu fault; PF, Papatea fault; JT, Jordan Thrust; HF, Hope fault; HDF, Hundalee fault; SJF, Stone Jug fault; CCF, Conway-Charwell fault zone; HFZ, Humps fault zone; PKF, Point Kean Fault; HST, Hikurangi subduction thrust. The red focal mechanism represents the epicenter of 2016 Kaikoura earthquake determined by the U.S. Geological Survey. The green focal mechanisms represent four $M_w > 6$ aftershocks. The cyan dots represent 2383 relocated aftershocks from the first 5.5 days (Kaiser et al., 2017). The dashed purple box outlines the region shown in Figure 2. The inset shows the study area (red dashed rectangle). The grey and cyan rectangles show the coverage of ALOS-2 and Sentinel-1, respectively. The white lines indicate the plate boundary faults. The yellow line represents the geometry of the HST from Williams et al. (2013).

radar imagery, and tsunami recordings). Kääb et al. (2017) showed the localized horizontal coseismic displacement field along the Kekerengu fault using images collected by the PlanetScope optical cubesat constellation. Kääb et al. (2017) observed ~10 m horizontal surface offsets on the Kekerengu fault and ~7 m on the Papatea fault. Clark et al. (2017) found highly variable coseismic coastal deformation ranging from −2.5 to 6.5 m from airborne light detection and ranging differencing. Hollingsworth et al. (2017) correlated Landsat-8 images from before and after the earthquake to obtain a complete horizontal coseismic displacement field covering the whole rupture. Hollingsworth et al. (2017) also analyzed seismic waveforms to determine fault slip on the Kekerengu fault and on a deeper offshore fault. Hamling et al. (2017) proposed a model involving slip on over 20 crustal fault segments and the Hikurangi subduction thrust to explain the observed coseismic displacements from both GPS and radar interferometry (interferometric synthetic aperture radar [InSAR]). Using a multiarray P wave back projection (BP) method, Zhang et al. (2017) showed the earthquake ruptured unilaterally along multiple faults to the northeast and found that the peak ground acceleration is well correlated with inferred release of short-period energy. Modeling teleseismic body waves and regional tsunami recordings, Bai et al. (2017) proposed simultaneous rupture on the subduction thrust and the upper crustal faults. This is also supported by joint

inversion of teleseismic waveform and space geodetic data (Wang et al., 2018). Heidarzadeh and Satake (2017), however, suggested that the tsunami was likely triggered by submarine landslides and fault slip on the subduction thrust. Cesca et al. (2017) examined regional and teleseismic data to reconstruct the ruptured fault geometry. Cesca et al. (2017) found that the upper crustal faults are connected with a low-angle splay thrust fault rather than the Hikurangi subduction thrust. Holden et al. (2017) studied local strong motion and high-rate GPS data and suggested that the Hikurangi subduction thrust most likely did not slip during the earthquake. Using only 21 local strong motion data, Zheng et al. (2018) estimated the source rupture process on multiple fault segments from the kinematic waveform inversion.

In this study, we combine seismic and geodetic data to study ground deformation of the 2016 Kaikoura earthquake and its relation to the geometrical complexity of faults and the rupture process at depth. We use InSAR data and radar offset measurements from multiple platforms to generate a complete three-dimensional coseismic displacement field. We analyze geodetic data to identify the ruptured faults, to constrain the source parameters and fault geometry. We examine the resolving power of our geodetic data to answer whether onshore geodetic data are sensitive to fault slip on the Hikurangi subduction thrust and the Point Kean fault. We also perform the BP analysis to image the rupture process of the Kaikoura earthquake. Finally, we discuss the implications of our results and examine remaining potential seismic hazards in the region.

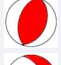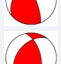## 2. Data and Methods

2.1. InSAR Data Processing

Satellite radar data acquired by the European Space Agency's C-band Sentinel-1 spacecraft paths (P73 and P52) and Japan Aerospace Exploration Agency L-band Advanced Land Observing Satellite-2 (ALOS-2) paths (P195 and P102) are used to generate ascending and descending coseismic interferograms. The main parameters of SAR images used are shown in the Table S1. We process the ALOS-2 and Sentinel-1 data from level 1.1 products with the traditional two-pass differential SAR interferometry method using the GAMMA software package. We use the 1 arc-sec Shuttle Radar Topography Mission digital elevation model (SRTM DEM) (Farr et al., 2007) to simulate and remove topographic phase and apply multilooking (20 × 4 for Sentinel-1 and 8 × 37 for ALOS-2 ScanSAR data) to increase the signal-to-noise ratio. To account for possible long wavelength orbital errors and atmospheric errors, the unwrapped InSAR phase is detrended by fitting a quadratic polynomial surface to GPS values that are located in the far field (>110 km) of the rupture.

We choose not to use the C-band Sentinel-1 interferograms in the study because they are decorrelated in most regions due to high deformation gradients. We use the L-band ALOS-2 interferograms, which have a better interferometric quality that enable us to unwrap to close to the fault ruptures. To complement the InSAR measurements, we calculate range and azimuth pixel offsets from both Sentinel-1 and ALOS-2 data. After coregistering two single-look complexes acquired before and after the mainshock, we calculate the image offsets using a standard SAR intensity tracking method. We estimate the offset fields using almost square search patches of 40 × 185 pixels (range × azimuth) for the ALOS-2 data (about 500 m × 500 m windows) and of 300 × 60 pixels for the Sentinel-1 data (about 700 × 700 m windows). To maintain a similar pixel spacing with the InSAR measurement, the offsets are estimated for every 8 range and 37 azimuth pixels in the ALOS-2 data, and for every 20 range and 4 azimuth pixels in the Sentinel-1 data. In addition to the actual coseismic surface displacement, the range offsets also include geometrical offsets in rugged terrain areas, which are removed using the SRTM DEM. To further reduce the noise, a median filter (8 × 8) is used in the calculated offsets. We combine both ascending and descending image offsets and InSAR measurement and use a weighted least squares inversion with the full variable unit vectors to derive a complete 3-D surface displacement map (Feng et al., 2017). The relative weight of different data sets is calculated based on their uncertainties.

2.2. Fault Slip Modeling

We subsample the descending and ascending unwrapped ALOS-2 interferograms using an algorithm considering both fringe rate and coherence (Feng et al., 2015), while subsampling image offsets using the quadtree method (Jónsson et al., 2002). Our preferred model is found by joint inversion of both continuous and campaign GPS data (Hamling et al., 2017), ALOS-2 unwrapped interferograms, and Sentinel-1 and ALOS-2 image offset measurements. These SAR data include 21 days of postseismic deformation. However, the

Table 1
Information About the Estimated Source Parameters of Model I

Fault	Length (km)	Width (km)	Strike (°) bounds, optimal value	Dip (°)	Rake (°) bounds, optimal value	Moment (N m)	M_w	Focal mechanism	Thrust percentage
HFZ	34	16	[242–273], 256	70	[176–180], 179	2.35×10^{19}	6.88		2%
CCF	26	20	[191–201], 195	50	[77–90], 85	3.67×10^{19}	7.01		87%
SJF	14	10	[338–343], 341	50	[2–8], 5	1.83×10^{18}	6.14		30%
HDF	46	20	[183–235], 206	50	[64–90], 75	5.0×10^{19}	7.10		82%
PF	30	20	[149–193], 172	50	[20–90], 50	1.23×10^{20}	7.36		60%
HF-JT-KF-NF	152	25	[210–251], 230	30–50[b]	[130–174], 158	5.0×10^{20}	7.77		29%
All	-	-	218[a]	44[a]	131[a]	7.35×10^{20}	7.88		42%

[a]The calculation is weighted by the moment.   [b]The value is varying along the strike on different faults.

amount of afterslip does not seem to contribute significantly. The data sets used in modeling are listed in the Table S2. The fault slip distribution is estimated following a two-step inversion approach. We first set the strike and surface location of the model faults following the rupture trace mapped from the image offsets. We try to use a fault geometry as simple as possible and found that six fault segments can reasonably represent the surface fault trace (Model I). We also build another two fault geometries to examine whether these geodetic data are able to reliably resolve fault slip on the Hikurangi subduction thrust (Model II) and the Point Kean fault (Model III). With the guidance from previous geological studies (Langridge et al., 2016; Litchfield et al., 2014), we bound the range of dip angles on each segment to within 30° of a priori values and search for the best fit uniform dip angle and slip on those fault segments in a homogeneous, elastic half-space, assuming a Poisson ratio of 0.25 and a shear modulus of 30 GPa (Okada, 1985). We determine the relative weighting between different SAR data sets in terms of the uncertainties estimated from the far-field area without seismic deformation. For simplicity, we use the error variance to weigh different data sets and assume that they are independent (W. Xu et al., 2016). Then, we optimize by trial and error the dip angle by running several distributed-slip inversions over a limited range of dip angles using a linear inversion. Following a similar approach, we optimize the depth-distribution of dip angles of the Hope, Jordan Thrust, Kekerengu, and Needles faults. We find that a listric geometry of these faults, with shallowing dip angles at depth, further reduces the misfit between the modeled and observed coseismic displacements (Table 1). Laplacian smoothing is applied between adjacent fault patches to avoid abrupt variations in slip. We utilize the L-curve method to determine the optimal smoothing factors, which consider the trade-off between the roughness of the fault slip and the data misfit. In the modeling, we not only invert for right- and left-lateral fault slips but also estimate fault thrust-slip component on each fault. The best fit fault parameters are listed in Table 1.

2.3. Back Projection With Slowness Calibrations

We image the kinematic rupture process of the Kaikoura earthquake using the BP approach. The BP technique relies on regional arrays of broadband seismometers and models the seismic wavefield to determine the rupture properties of large earthquakes such as rupture length, direction, speed, and segmentation (Kiser & Ishii, 2017). We perform the BP analysis on coherent P wave seismograms recorded by approximately 180 broadband seismic stations of the China Array within teleseismic distance across southeastern China (Figure S1). The data are filtered between 0.5 and 2 Hz and aligned on the first P wave arrivals with a multi-channel cross-correlation technique. We apply the Multitaper-Music array processing technique (Meng et al., 2011), which resolves closely spaced sources and produces a sharper image of the rupture process than the standard beamforming approach (e.g., Ishii et al., 2005). We adopt the "reference window" strategy (Meng, Ampuero, Luo, et al., 2012) to mitigate "swimming" artifacts, a systematic bias that manifests as

high-frequency energy moving toward the array. To calibrate the BP spatial bias due to approximating the 3-D Earth structure with a 1-D reference model, we also apply a slowness (ray parameter) calibration procedure using the location errors of five aftershock BPs (Meng et al., 2016). In the BP analysis, the alignment procedure provides a static correction to account for the traveltime variations due to 3-D Earth structures, assuming that the first *P* phase pulse originates from a reference hypocenter location. In this study, we adopt National Earthquake Information Center catalogue for reference hypocenter and aftershock locations. The subsequent ruptures are tracked based on their differential traveltimes relative to the reference location. As the teleseismic traveltime is not sensitive to small depth differences, the BP is performed at a constant depth of 15 km. We provide a test that involves imaging aftershocks assuming different focal depths. We find that teleseismic BP maps only a fraction of the source-depth difference into its horizontal location (Figure S2). Considering the seismogenic depth extent of the MFS is approximately 20 km, this choice of a constant focal depth has a negligible effect on the horizontal BP-inferred source locations. This strategy of "hypocenter alignment" is adequate when the rupture remains close to the hypocenter but is less effective for large earthquakes. For the Kaikoura earthquake sequence, the apparent source locations inferred from aftershock BPs confirm a systematic westward bias away from the National Earthquake Information Center catalogue locations. Here we apply a slowness (ray parameter) correction that accounts for the traveltime errors of sources distant from the epicenter (Meng et al., 2016). The slowness correction can be effectively calibrated using the location errors of the aftershocks. We derive the 2-D vector slowness correction term based on five moderate aftershocks located around the northeastern end of the Kaikoura earthquake (Figure 1). To understand the performance of BP in the presence of changing focal mechanisms, we conduct synthetic tests of BP using empirical Green's function of both thrust and strike-slip aftershocks. We generate synthetic seismograms composed of multiple sources in the study area as shown in Figure S3. The rupture involves three stages: a thrust faulting on the Humps fault, a strike-slip rupture on the Hope fault and a thrust faulting on the Papatea fault. We back project the synthetic seismograms and compare the BP radiators with our input sources. According to Figure S3, our BP images recover the input sources despite the change of the mechanisms. Therefore, we consider that the BP source locations are not significantly affected by variations of focal mechanisms. The BP power is, on the other hand, subject to the change of the radiations pattern and focal mechanisms. Therefore, the BP power may not directly reflect the relative moment partitioning between individual fault segments.

2.4. Coulomb Failure Stress Change Calculation

Coulomb failure stress change can be defined as follows (Lin & Stein, 2004): $\Delta\text{CFS} = \Delta\tau + \mu^{'}\Delta\sigma$, where $\Delta\tau$ and $\Delta\sigma$ represent the changes in the shear (positive along slip direction) and normal stresses (positive for unclamping) on the receiver fault, respectively, and $\mu^{'}$ is the effective coefficient of friction. We choose $\mu^{'} = 0.4$ in the stress calculations for the analysis and discussion. We use our estimated dislocation model as the source model. For the receiver faults, we download the faults' geometry and location from the Institute of Geological and Nuclear Sciences active fault database (Langridge et al., 2016) and calculate the ΔCFS at depths between 0 and 25 km.

3. Results

3.1. 3-D Deformation Field

We successfully unwrapped the L-band ALOS-2 interferograms for coseismic deformation except in some regions close to the faults (Figure S4). We calculate range and azimuth offsets using the image offset tracking method to retrieve near-fault coseismic ground deformation (Michel et al., 1999) (Figures S5–S7). However, very dense interferometric fringes observed in the C-band Sentinel-1 interferograms make phase unwrapping challenging, especially in highly deformed regions near the ruptured faults. We invert Sentinel-1 offsets, ALOS-2 offsets, and ALOS-2 interferograms to estimate the three-dimensional surface displacement field of the Kaikoura earthquake by a weighted least squares approach (Fialko et al., 2001). The three-dimensional displacements reveal a complex ground deformation field and multiple displacement discontinuities across the ruptured faults (Figures 2, 3, and S8). The surface displacements are larger in the northern part of the rupture than in its southern section. The vertical displacement agrees well with the coastal uplift light detection and ranging data (Figure S9). Coseismic ground displacements of up to 10 m horizontally and about 2 m vertically are observed along the Kekerengu fault (Figure 2). The region west of the Papatea fault moved primarily
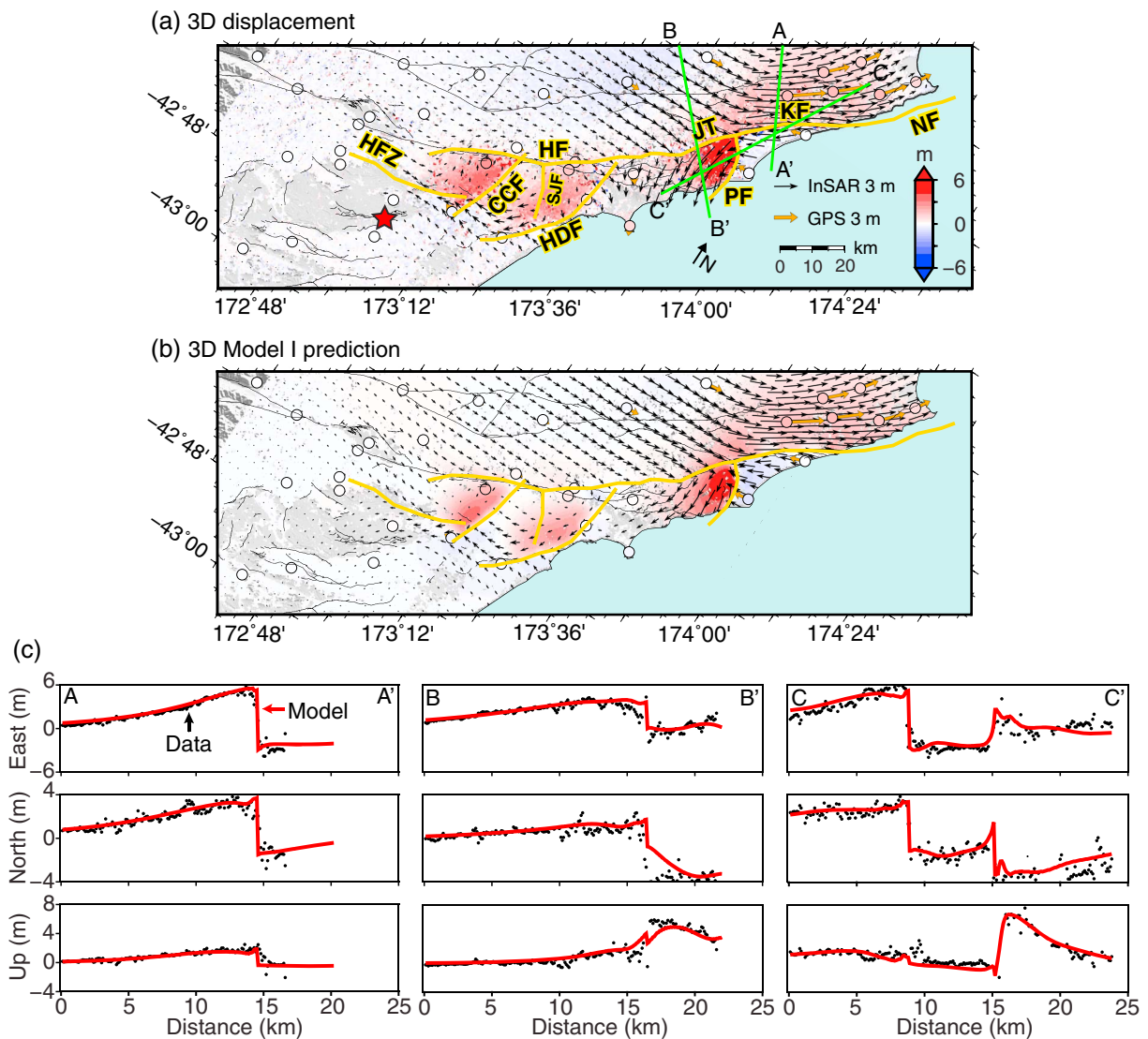
Figure 2. Observed and modeled three-dimensional interferometric synthetic aperture radar deformation field of the 2016 Kaikoura earthquake. (a) Three-dimensional deformation field created from ALOS-2 interferograms and range and azimuth offsets from both Sentinel-1 and ALOS-2 spacecraft. The black arrows show the horizontal component, and the colors represent the vertical component. The brown arrows represent GPS horizontal motion. The color-coded circles show the GPS vertical motion with the same color scale. The red star indicates the location of U.S. Geological Survey epicenter. (b) Corresponding Model I prediction. (c) Observed (black) and modeled (b) displacements along profiles A-A′, B-B′, and C-C′.

to the south and was uplifted by about 8 m during the earthquake, causing a sharp discontinuity across the fault. Closer to the epicenter, we find that the Hope fault and the Humps fault zone are dominated by right-lateral horizontal motion, while surface uplift of approximately 3 m is seen along the Hundalee fault and the Conway-Charwell fault zone (Figure 2). These results suggest that the earthquake initiated as a strike-slip rupture that propagated to the northeast causing extensive transpressional oblique faulting.

3.2. Coseismic Slip Distribution Model

The estimated average dip angles of the rupture segments are generally consistent with those in the New Zealand fault database (Litchfield et al., 2014) (see Tables 1 and S3). Hamling et al. (2017) and Wang et al. (2018) fixed the dip angle of 80 in the modeling, while our optimal dip along the Needles and Kekerengu faults is determined from the inversion of our geodetic constraints (InSAR, offsets, and GPS). However, our slip distribution patterns and magnitudes on these faults are quite similar. The best fit fault slip distribution model shows that the ruptures involve a mixture of fault slip motions (Figure 4). Distinct thrust-slip patches (over
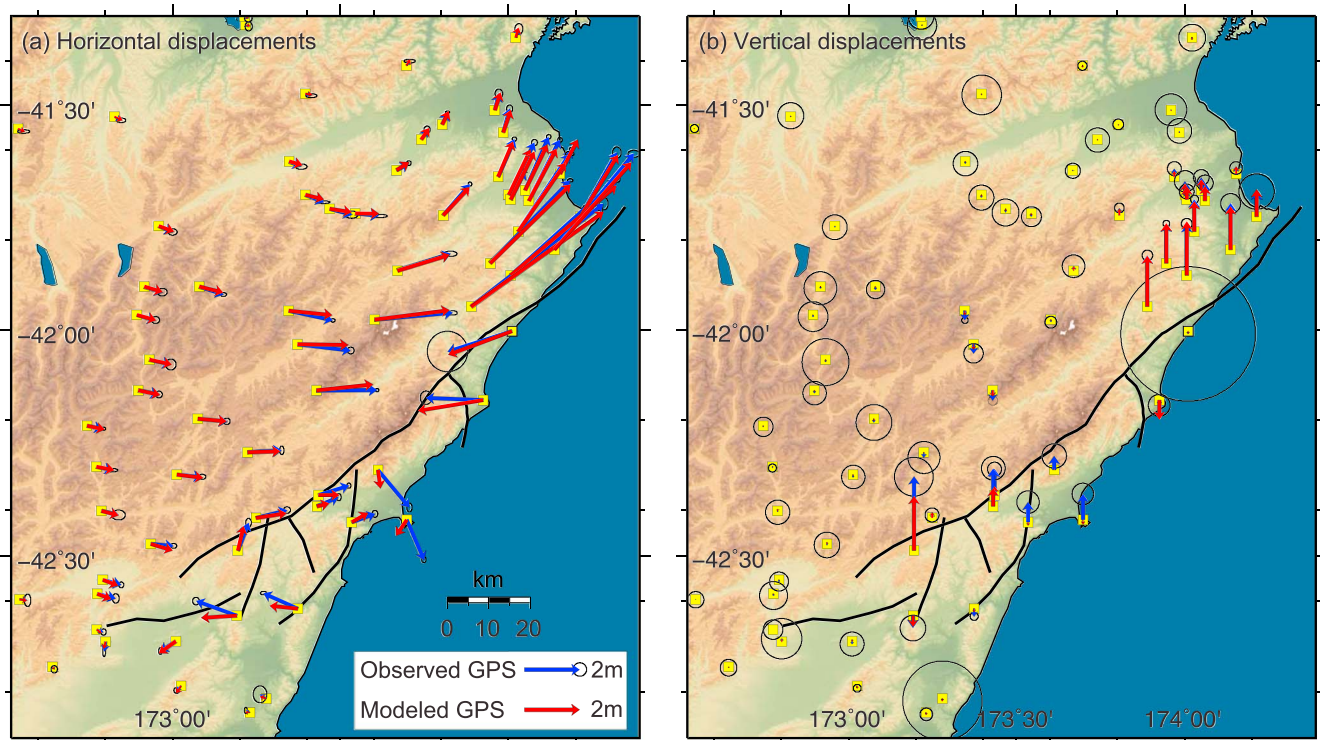
Figure 3. Coseismic Global Positioning System (GPS) offsets of the 2016 Kaikoura earthquake and the modeling result. The blue and red arrows show observed and modeled (a) horizontal and (b) vertical GPS displacements, respectively.

60%) at shallow depths are seen on the branching Conway-Charwell fault zone, Hundalee fault, and Papatea fault segments, while the thrust component is small on the other ruptured segments (Figure 4 and Table 1). The maximum thrust slip of up to 18 m occurred on the Papatea fault at shallow depth near the intersection with the Kekerengu fault (Figure 4). Different from previous findings (Hamling et al., 2017; Hollingsworth et al., 2017), the ground movements around the Papatea fault could be well modeled using our elastic dislocation model, thanks to the optimized fault geometry, without appealing to off-fault anelastic deformation. Predominantly shallow right-lateral strike slip is seen on the Humps fault zone (the ratio between strike and thrust slip is 98%). Right-lateral strike slip observed on the north-east striking Humps fault zone, the Conway-Charwell fault zone, and the Needles fault is concentrated within the upper 12 km. About 10 m of slip occurred at the surface on the Kekerengu fault, consistent with field observations and other published work (Litchfield et al., 2016; Hamling et al., 2017; Hollingsworth et al., 2017; Kääb et al., 2017). The peak strike slip of 15 m is seen at depths between 2 and 10 km (Figure 4). The Hope fault, which has a rapid 20–25 mm/year slip rate (Van Dissen & Yeats, 1991) along the Conway segment, experiences the least coseismic fault slip with an average of 3 m. A component of left-lateral strike slip is found on the branching, north striking oblique thrust faults, namely, the Conway-Charwell fault zone, the Stone Jug fault, the Hundalee fault, and the Papatea fault, mostly at relatively shallow depths from the surface to about 8 km (Figure 4). The slip at greater depth, however, is less well constrained by the data (Figure S10). The geodetically derived focal mechanism obtained by summing moment tensors of the six subevents is remarkably consistent with Global Centroid Moment Tensor and other published work (Cesca et al., 2017; Duputel & Rivera, 2017; Hamling et al., 2017; Hollingsworth et al., 2017; Kaiser et al., 2017). The geodetic moment of 7.35×10^{20} N m is equivalent to M_w 7.88 (see Table 1). This value is about 4% higher than the available seismic estimates. The estimated average coseismic stress drop following Noda et al. (2013) is 34 MPa, which is close to the estimated value of Kaneko et al. (2017).

3.3. The Resolvability of Fault Slip on the Hikurangi Subduction Thrust and the Point Kean Fault

Our Model II, which involves the Hikurangi subduction thrust, shows very similar slip distribution patterns and values on the Humps fault zone, Conway-Charwell fault zone, Jordan Thrust, Stone Jug fault, Kekerengu fault,
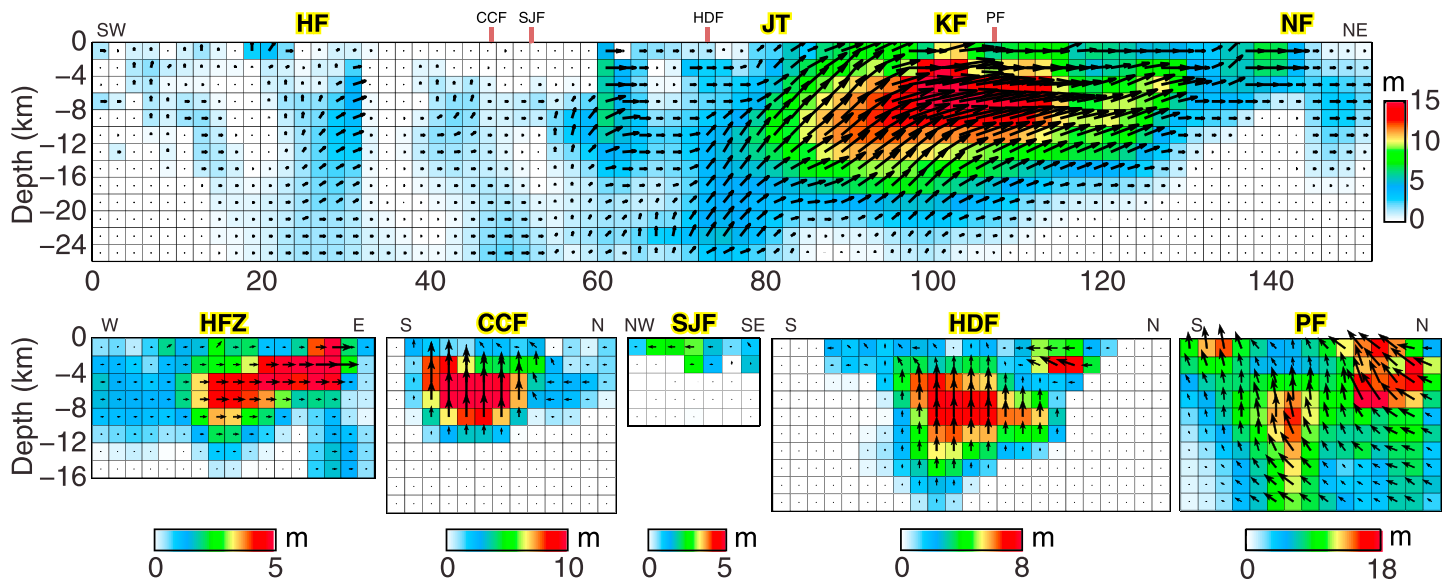
Figure 4. Finite fault slip model of the 2016 Kaikoura earthquake (Model I). The colors represent the amplitude of the slip vectors. The black arrows denote the slip direction the hanging wall.

and the Needless fault as those of our Model I. The fault slip on the Hundalee fault and on the southern part of the Papatea fault decreases significantly. The maximum inverted fault slip of 8 m on the Hikurangi mega-thrust is found between the Hundalee fault and the Papatea fault at depths from 10 to 30 km offshore Kaikoura (Figure 5a). Two additional zones of slip of up to 5 m are found beneath the northern section of the Hope fault and the Jordan Thrust. A checkerboard test, however, suggests that the estimated slip is not reliably recovered using only the onshore geodetic data (Figure S11). The far-field GPS data are not better fit by Model II neither (Figure S12). Therefore, the inverted thrust slip on the Hikurangi subduction thrust is not well constrained. This is consistent with the findings of Clark et al. (2017) and Cesca et al. (2017), who were also not able to uniquely resolve slip on the Hikurangi megathrust. The updated Model II has a geodetic moment of 8.95×10^{20} N m corresponding to M_w 7.94. Our Model III shows that up to 10 m slip on the Point Kean fault, despite that fault slip distribution on other major faults, is very similar to that of the Model II (Figure 5b). As the Point Kean fault is mostly located offshore, our checkerboard test shows that
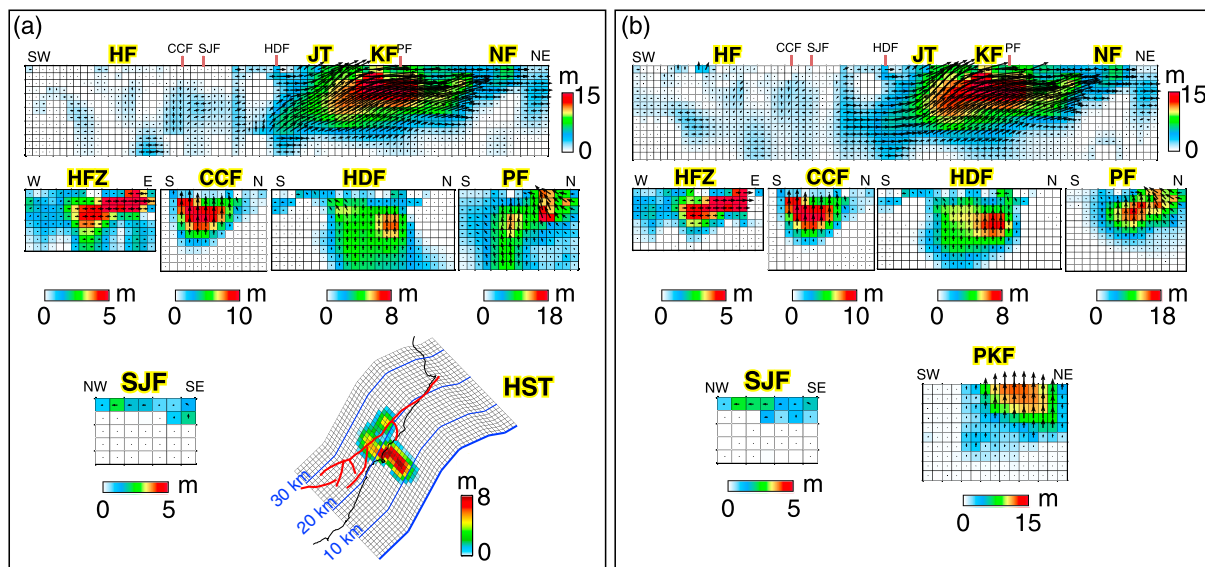
Figure 5. Same as Figure 4 but for other possible slip models that allow for slip on (a) the Hikurangi subduction thrust (Model II) and (b) the Point Kean fault (Model III).
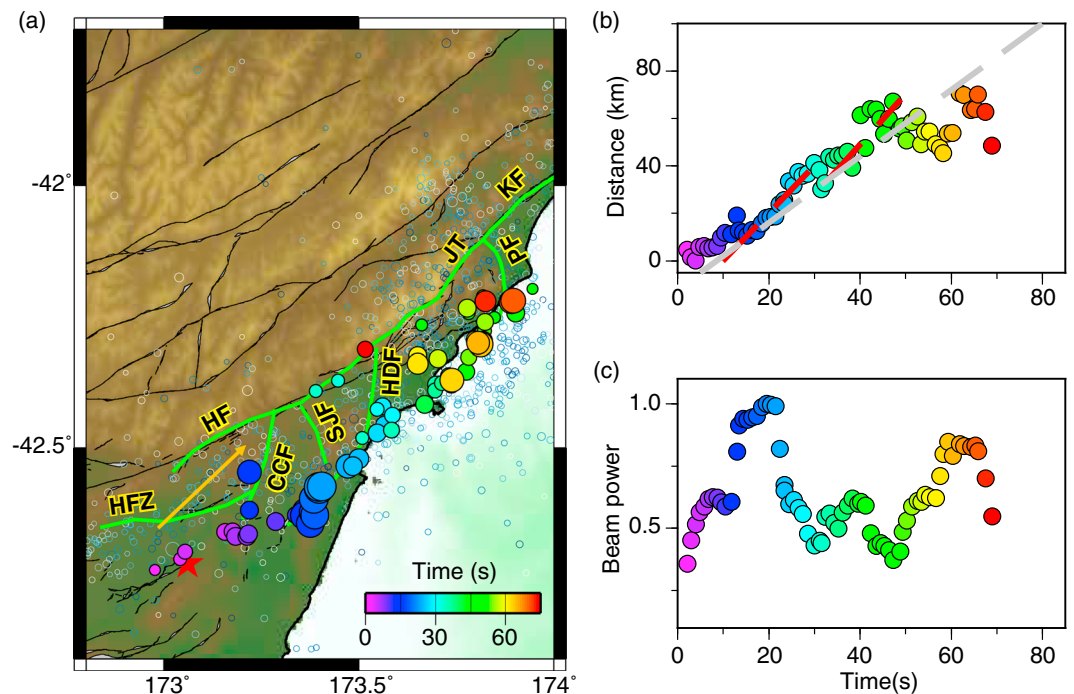
Figure 6. (a) High-frequency radiators (colored circles) imaged by the slowness-calibrated back projection method on data recorded by the China Array, with circle size proportional to relative amplitude of high-frequency radiation and symbol color intensity representing rupture time with respect to mainshock origin time (unit, s). The red star denotes the National Earthquake Information Center epicenter. (b), Time propagation as a function of time along the direction of Hope-Jordan Thrust-Kekerengu fault system (orange arrow in panel a). The grey and red dashed lines represent rupture speeds of 1.4 and 2 km/s, respectively. (c) Relative beam power as a function of time.

the estimated slip is not reliably recovered using only the onshore geodetic data (Figure S13). Therefore, even though part of the Point Kean fault was mapped during the field work and whether fault slip occurred on the Hikurangi subduction thrust (Furlong & Herman, 2017), it is clear that the onshore geodetic data alone cannot reliably resolve fault slip on these noncrustal thrust faults.

3.4. Rupture Properties of the 2016 Kaikoura Earthquake

The kinematic rupture process of the Kaikoura earthquake is effectively revealed by the BP approach. The calibrated teleseismic BP reveals that the earthquake initiated near the Humps fault zone and propagated northeastward over 100 km, stepping and branching through a complex fault system. The most coherent teleseismic high-frequency radiation mainly involves oblique-reverse faulting along the Conway-Charwell fault zone, the Hundalee fault, and the Papatea fault (Figure 6a). This is contrast to the predominant contribution of the strike-slip rupture along Humps fault zone, Hope fault, and Kekerengu fault to the near-source high-frequency radiation suggested by a preliminary analysis of local strong motion data (Kaiser et al., 2017). In the first 10 s, the radiators stalled without clear propagation, indicating a slow initiation on the Humps fault zone north of the epicenter. From 10 to 20 s, the rupture extended along the Conway-Charwell fault zone thrust at a speed of approximately 2.0 km/s (Figure 6b). The high-frequency teleseismic energy radiation reached its maximum at the junction of the Conway-Charwell fault zone and the Hope fault (Figure 6c). At 25 s, the radiators abruptly stepped from the Hope fault to the Hundalee fault. They then propagated toward the north along Hundalee fault at a speed of 2.0 km/s for about 10 s. A second jump occurred from the Hundalee fault to the PF at 35 s, followed by northward propagation along the PF. A second energy peak emerged near the PF between 60 and 70 s. While the overall rupture speed along the main direction of the Kaikoura fault system is relatively slow, 1.4 km/s, the speed along each individual segment is significantly faster. This observation is consistent with the kinematic model based on local strong motion data (Holden et al., 2017), which suggests rupture speed around 2 km/s on multiple fault segments including the Humps-Hundalee fault and the Kekerengu-Needle fault. Beyond 70 s, the BP radiators appear scattered
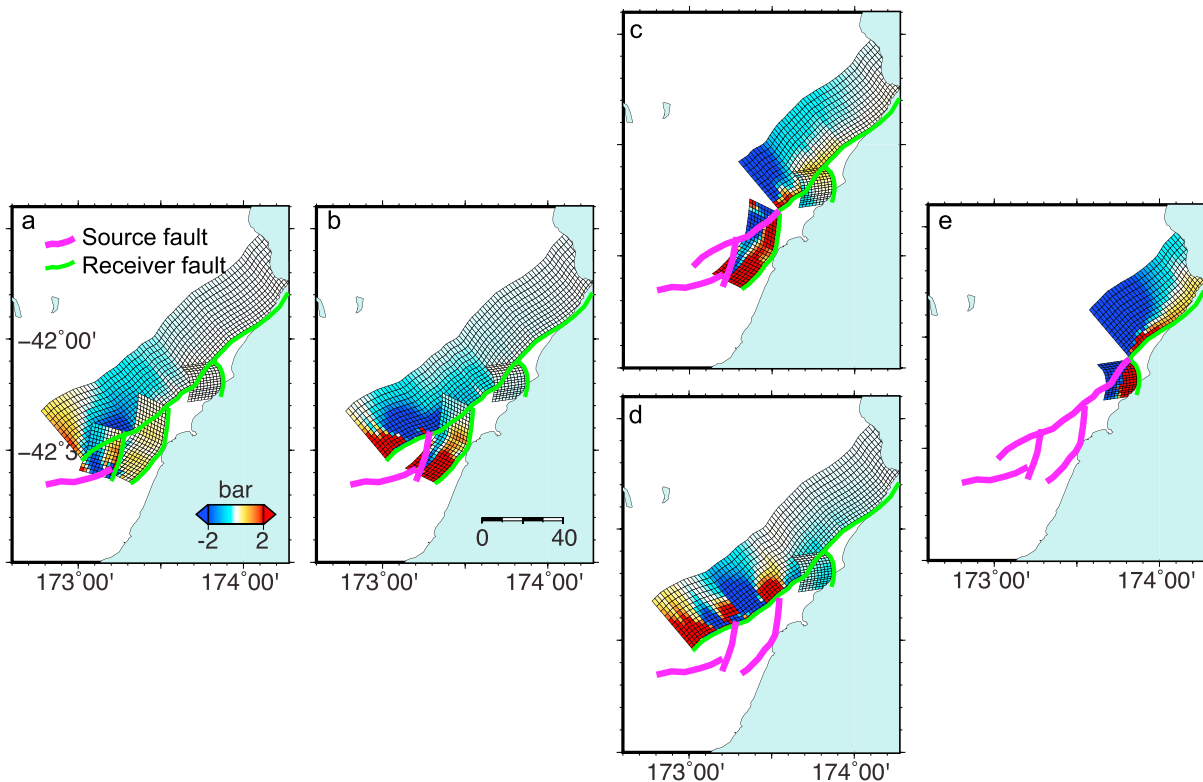
Figure 7. Static Coulomb failure stress changes (ΔCFS) induced by slip of part of the rupture (surface traces of activated faults indicated by magenta solid curves; slip and rake as shown in Figure 4) on the fault segments that rupture later (surface traces indicated by green dashed curves), following a rupture sequence (from left to right) of the 2016 Kaikoura earthquake inferred from back projection. It is difficult to distinguish if the rupture processed from (b) to (c) or from (b) to (d) from the static ΔCFS calculations. Note that the Stone Jug fault is not considered in the calculation.

and do not conform to a particular fault trace, possibly due to the dominance of coda waves. The kinematic rupture at this stage is likely to continue along the Kekerengu-Needles faults as suggested by the coseismic slip inferred by our geodetic observation.

4. Discussion and Conclusions

Past earthquakes, including the 1992 Landers earthquake (Sieh et al., 1993), 1999 Hector Mine earthquake (Jónsson et al., 2002), and 2012 east Indian Ocean earthquake (Meng, Ampuero, Stock, et al., 2012), have highlighted the possibility of rupture on branched fault systems. Particularly, fault branching into the compressive quadrant and rupture transfer between three almost orthogonal strike-slip faults have been observed in the 2012 Sumatra earthquake (Meng, Ampuero, Stock, et al., 2012). The last earthquake of comparable magnitude that occurred in the MFS was the 1848 M_w 7.4–7.7 Marlborough earthquake (Mason & Little, 2006). Fault branching associated with the 1848 earthquake was observed along the southern section of the Awatere fault near Molesworth station. The complex pattern of fault slip at the surface caused variable off-fault deformation forming numerous scarps (Mason & Little, 2006). During 2010–2012, an extended sequence of four $M_w \geq 6$ earthquakes took place in the Canterbury region, around 120 km south of the 2016 Kaikoura epicenter, in which complex ground deformation and fault branching involving multiple strike-slip and secondary thrust fault movements were observed (Bannister & Gledhill, 2012; Elliott et al., 2012). However, none of the above earthquakes show a rupture process that is as complex as the 2016 Kaikoura earthquake. Regional moment tensor solutions of aftershocks independently support the rupture complexity, showing a dominance of strike-slip mechanisms near both ends of the rupture and more oblique and reverse faulting mechanisms along the central section (Cesca et al., 2017; Kaiser et al., 2016). However, aftershock focal mechanisms tend to be more a reflection of the state of stress in the adjacent crust than the geometry of individual rupture segments (e.g., Hardebeck, 2010, 2012).
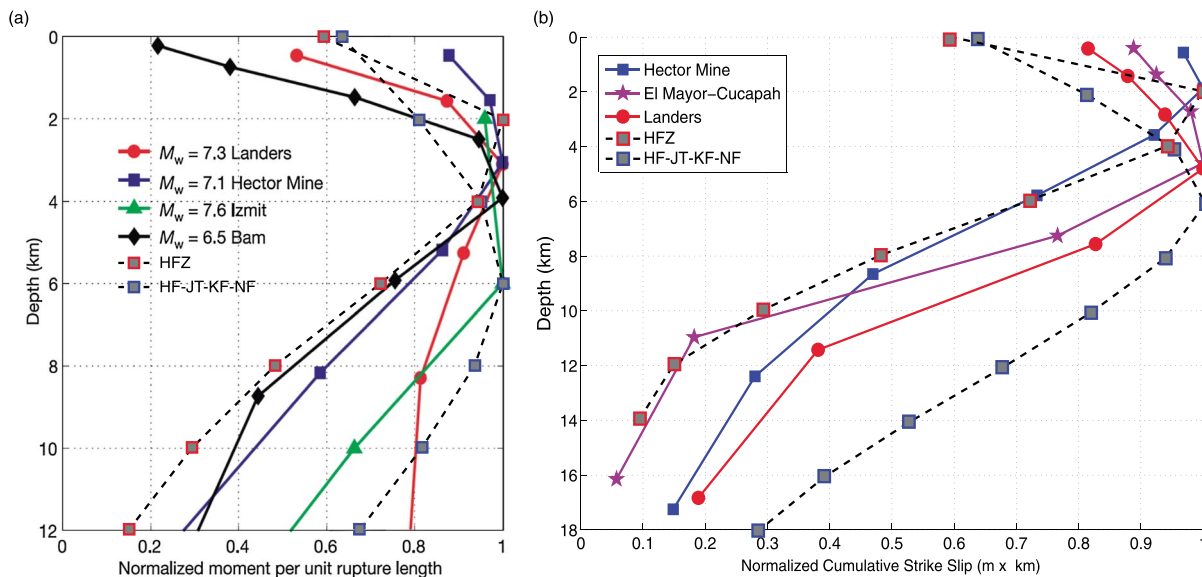
Figure 8. Distributions of coseismic slip for several ~M7 strike-slip earthquake integrals along the rupture length, normalized by their max value as a function of depth (Fialko et al., 2005) together with the Humps fault zone and Hope-Jordan Thrust-Kekerengu-Needles fault segments. The figure is modified after (a) Fialko et al. (2005) and (b) X. Xu et al. (2016), respectively.

To shed light on the mechanics of the rupture process, we computed static CFS changes induced by initial segments of the rupture on the subsequently ruptured fault segments, comparing different plausible scenarios for the rupture sequence (Figure 7). The calculations are based on our finite source Model I, which does not include coseismic slip on the subduction thrust, in contrast to previous studies (Hamling et al., 2017; Wang et al., 2018). While further validation by dynamic stress modeling is warranted (e.g., Aochi et al., 2005; Bai & Ampuero, 2017; Douilly et al., 2015), the static calculations support the following scenario. The Kaikoura earthquake rupture nucleated near the Humps fault zone and branched onto the Conway-Charwell fault zone, inducing stresses that favored rupture nucleation near the southern end of both the Hope fault and Hundalee fault. This is consistent with the northward rupture along the Hundalee fault imaged by BP. The rupture propagated along the Jordan fault, the Kekerengu fault, and the Needles fault and triggered slip on the PF. Together with previous studied earthquakes of the MFS and the Canterbury region, the Kaikoura earthquake further emphasizes the geometric complexity of fault traces and associated heterogeneous crustal deformation in the region.

Rupture speed, principal stress directions, and ratios of components in the prestress field are three important parameters that control fault branching (Poliakov et al., 2002). Based on the inferred principal stress directions from stress tensor inversions in northern South Island, Townend et al. (2012) found the principal compressional stress in the area of the ~55° striking Kekerengu fault is oriented about 115°. Therefore, there is a 60° angle between the most compressive stress and the Kekerengu fault. The background stress oriented at this steep angle is favorable for driving slip on the Papatea fault and other north striking faults. This suggests that the conjugate Kekerengu fault and Papatea fault in the MFS are relatively weak faults; that is, they operate at average shear stresses well below dry Byerlee's friction. Similar weak fault segments (e.g., Fort Tejon and Mojave segments) have also been found along the San Andreas Fault in a comparably transpressional tectonic regime (Hardebeck & Michael, 2004).

Shallow slip deficits (SSD) have been reported in several large strike-slip events (Fialko et al., 2005). Various mechanisms have been proposed to explain the SSD (Fialko et al., 2005; Kaneko & Fialko, 2011). Our fault slip model shows a reduced slip at the shallow (0–3 km) depth on the Humps fault zone and the Hope-Jordan Thrust-Kekerengu-Needles fault segments (Figure 8). These two segments are dominated by strike-slip motion during the 2016 Kaikoura earthquake (Table 1). The SSD possibly results from inelastic failure in the shallow crust and a lack of data coverage close to the Humps fault zone (X. Xu et al., 2016). Field observations, however, suggest extensive displaced landforms, such as scattered small traces, landslides, liquefaction, and lateral spreading occurred near the Humps fault zone and Hope fault. This might indicate the strong ground
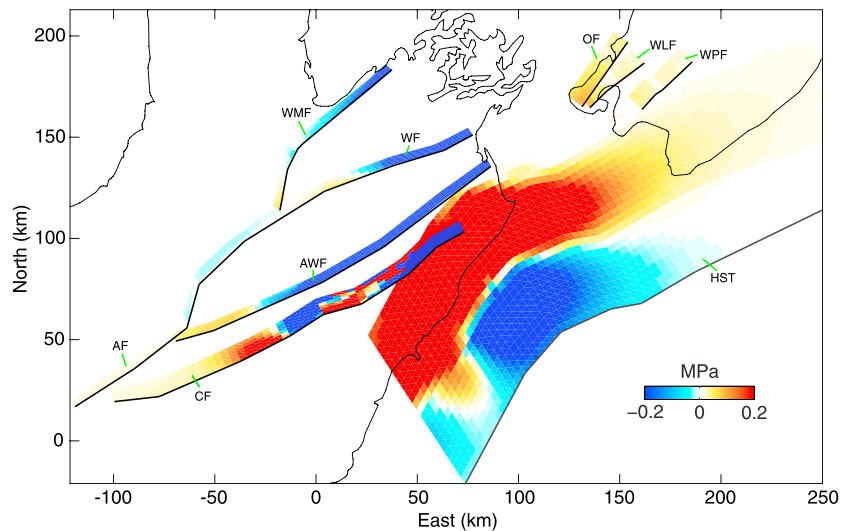
Figure 9. Calculated Coulomb failure stress changes (ΔCFS) on major faults after the Kaikoura earthquake. The mapped major faults are labeled, and the black thick line representing the top edge of the fault: OF, Ohariu fault; WLF, Wellington fault; WPF, Wairarapa fault; WMF, Waimea fault; HST, Hikurangi subduction thrust. Failure is favored if the ΔCFS is positive and discouraged if negative. Note that the geometry of the HST is modified from Williams et al. (2013) with the dip angle set to 15° for simplicity. The rake varies down-dip (from 90 degrees at <15 km depth, to more equal components of right-lateral strike slip and dipslip). Other major faults from the Institute of Geological and Nuclear Sciences active faults database.

motion produced distributed inelastic deformation that is responsible for the inferred SSD. In contrast, the SSD along other modeled transpressional segments in this study is weak. One possible reason could be that the deep thrust motion has altered the shallow stress field, triggering shallow strike slip that compensates the SSD. Together with the relatively slow rupture speed, the occurrence of inelastic deformation (Kaneko et al., 2017), and the existence of structural complexity, we suggest that the combination of these effects may be the cause for the slow propagation speed of this complex rupture.

The 2016 M_w 7.8 Kaikoura earthquake altered the shear and normal stress on surrounding active faults (Figure 9). Static Coulomb failure stress changes (ΔCFS) are calculated to have been decreased on other major northeast-striking faults of the MFS. The rupture zone of the 1848 M_w 7.4–7.7 earthquake on the northern segment of Awatere fault fall in the stress shadow of the Kaikoura earthquake. However, the major right-lateral strike-slip Alpine fault that has ruptured four times in the past 900 years (Berryman et al., 2012), the southern sections of the Awatere fault and the Clarence faults in the South Island lie in areas of increased calculated Coulomb stress from the Kaikoura earthquake. In the North Island, the Ohariu, Wellington, and Wairarapa faults are brought closer to failure. A recent study suggests that the 2016 Kaikoura earthquake triggered slow slip movement along the Hikurangi subduction thrust extending from the north part of the South Island to off the east coast of the North Island (Wallace et al., 2017). The subduction thrust located in the region east of Wellington, however, seems to be locked and continues to accumulate stress (Wallace & Beavan, 2010; Witze, 2017). The Kaikoura earthquake added over 0.6 MPa in the deeper, southernmost portion of the locked asperity, while producing very modest and mostly negative Coulomb stress changes further north. Thus, the extensive slow slip episode on the shallow northern Hikurangi megathrust was likely triggered by dynamic stresses (Wallace et al., 2017). Our stress calculations suggest that the seismic hazard of future great earthquakes on several major faults on the South Island and in the south end of the North Island is high.

References

Aochi, H., Scotti, O., & Berge-Thierry, C. (2005). Dynamic transfer of rupture across differently oriented segments in a complex 3-D fault system. *Geophysical Research Letters*, *32*, L21304. https://doi.org/10.1029/2005GL024158

Bai, K., & Ampuero, J.-P. (2017). Effect of seismogenic depth and background stress on physical limits of earthquake rupture across fault step overs. *Journal of Geophysical Research: Solid Earth*, *122*, 10,280–10,298. https://doi.org/10.1002/2017JB014848

Bai, Y., Lay, T., Cheung, K. F., & Ye, L. (2017). Two regions of seafloor deformation generated the tsunami for the 13 November 2016, Kaikoura, New Zealand earthquake. *Geophysical Research Letters*, *44*, 6597–6606. https://doi.org/10.1002/2017GL073717

Bannister, S., & Gledhill, K. (2012). Evolution of the 2010–2012 Canterbury earthquake sequence. *New Zeal. Journal of Geology and Geophysics*, *55*(3), 295–304. https://doi.org/10.1080/00288306.2012.680475

Berryman, K. R., Cochran, U. A., Clark, K. J., Biasi, G. P., Langridge, R. M., & Villamor, P. (2012). Major earthquakes occur regularly on an isolated plate boundary fault. *Science*, *336*(6089), 1690–1693. https://doi.org/10.1126/science.1218959

Cesca, S., Zhang, Y., Mouslopoulou, V., Wang, R., Saul, J., Savage, M., et al. (2017). Complex rupture process of the M_w 7.8, 2016, Kaikoura earthquake, New Zealand, and its aftershock sequence. *Earth and Planetary Science Letters*, *478*, 110–120.

Clark, K. J., Nissen, E. K., Howarth, J. D., Hamling, I. J., Mountjoy, J. J., Ries, W. F., et al. (2017). Highly variable coastal deformation in the 2016 Mw7.8 Kaikōura earthquake reflects rupture complexity along a transpressional plate boundary. *Earth and Planetary Science Letters*, *474*, 334–344.

Douilly, R., Aochi, H., Calais, E., & Freed, A. M. (2015). Three-dimensional dynamic rupture simulations across interacting faults: The *Mw*7.0, 2010, Haiti earthquake. *Journal of Geophysical Research: Solid Earth*, *120*, 1108–1128. https://doi.org/10.1002/2014JB011595

Duputel, Z., & Rivera, L. (2017). Long-period analysis of the 2016 Kaikoura earthquake. *Physics of the Earth and Planetary Interiors*, *265*, 62–66. https://doi.org/10.1016/j.pepi.2017.02.004

Elliott, J. R., Nissen, E. K., England, P. C., Jackson, J. A., Lamb, S., Li, Z., et al. (2012). Slip in the 2010–2011 Canterbury earthquakes, New Zealand. *Journal of Geophysical Research: Solid Earth*, *117*, B03401. https://doi.org/10.1029/2011JB008868

Farr, T. G., Rosen, P. A., Caro, E., Crippen, R., Duren, R., Hensley, S., et al. (2007). The shuttle radar topography mission. *Reviews of Geophysics*, *45*, RG2004. https://doi.org/10.1029/2005RG000183

Feng, G., Li, Z., Shan, X., Zhang, L., Zhang, G., & Zhu, J. (2015). Geodetic model of the 2015 April 25 Mw 7.8 Gorkha Nepal earthquake and Mw 7.3 aftershock estimated from InSAR and GPS data. *Geophysical Journal International*, *203*(2), 896–900. https://doi.org/10.1093/gji/ggv335

Feng, G., Jónsson, S., & Klinger, Y. (2017). Which fault segments ruptured in the 2008 Wenchuan earthquake and which did not? New evidence from near-fault 3D surface displacements derived from SAR image offsets. *Bulletin of the Seismological Society of America*, *107*(3), 1185–1200. https://doi.org/10.1785/0120160126

Fialko, Y., Simons, M., & Agnew, D. (2001). The complete (3-D) surface displacement field in the epicentral area of the 1999 Mw7.1 Hector Mine earthquake, California, from space geodetic observations. *Geophysical Research Letters*, *28*(16), 3063–3066. https://doi.org/10.1029/2001GL013174

Fialko, Y., Sandwell, D., Simons, M., & Rosen, P. (2005). Three-dimensional deformation caused by the Bam, Iran, earthquake and the origin of shallow slip deficit. *Nature*, *435*(7040), 295–299. https://doi.org/10.1038/nature03425

Furlong, K. P., & Herman, M. (2017). Reconciling the deformational dichotomy of the 2016 M_w 7.8 Kaikoura New Zealand earthquake. *Geophysical Research Letters*, *44*, 6788–6791. https://doi.org/10.1002/2017GL074365

Hamling, I. J., Hreinsdóttir, S., Clark, K., Elliott, J., Liang, C., Fielding, E., et al. (2017). Complex multifault rupture during the 2016 M_w 7.8 Kaikōura earthquake, New Zealand. *Science*, *356*(6334), eaam7194. https://doi.org/10.1126/science.aam7194

Hardebeck, J. (2010). Aftershocks are well aligned with the background stress field, contradicting the hypothesis of highly heterogeneous crustal stress. *Journal of Geophysical Research*, *115*, B12308. https://doi.org/10.1029/2010JB007586

Hardebeck, J. L. (2012). Coseismic and postseismic stress rotations due to great subduction zone earthquakes. *Geophysical Research Letters*, *39*, L21313. https://doi.org/10.1029/2012GL053438

Hardebeck, J. L., & Michael, A. J. (2004). Stress orientations at intermediate angles to the San Andreas Fault, California. *Journal of Geophysical Research*, *109*, B11303. https://doi.org/10.1029/2004JB003239

Heidarzadeh, M., & Satake, K. (2017). Possible dual earthquake-landslide source of the 13 November 2016 Kaikoura, New Zealand Tsunami. *Pure and Applied Geophysics*, *174*(10), 3737–3749.

Holden, C., Kaneko, Y., D'Anastasio, E., Benites, R., Fry, B., & Hamling, I. J. (2017). The 2016 Kaikōura earthquake revealed by kinematic source inversion and seismic wavefield simulations: Slow rupture propagation on a geometrically complex crustal fault network. *Geophysical Research Letters*, *44*, 11,320–11,328. https://doi.org/10.1002/2017GL075301

Hollingsworth, J., Ye, L., & Avouac, J. P. (2017). Dynamically triggered slip on a splay fault in the M_w 7.8, 2016 Kaikoura (New Zealand) earthquake. *Geophysical Research Letters*, *44*, 3517–3525. https://doi.org/10.1002/2016GL072228

Ishii, M., Shearer, P. M., Houston, H., & Vidale, J. E. (2005). Extent, duration and speed of the 2004 Sumatra-Andaman earthquake imaged by the Hi-Net array. *Nature*, *435*(7044), 933–936. https://doi.org/10.1038/nature03675

Jónsson, S., Zebker, H., Segall, P., & Amelung, F. (2002). Fault slip distribution of the 1999 M_w 7.1 Hector Mine, California, earthquake, estimated from satellite radar and GPS measurements. *Bulletin of the Seismological Society of America*, *92*(4), 1377–1389. https://doi.org/10.1785/0120000922

Kääb, A., Altena, B., & Mascaro, J. (2017). Coseismic displacements of the 14 November 2016 M_w7. 8 Kaikoura, New Zealand, earthquake using an optical cubesat constellation. *Natural Hazards and Earth System Sciences*, *17*, 627–639.

Kaiser, A., Balfour, N., Fry, B., Holden, C., Litchfield, N., Gerstenberger, M., et al. (2017). The 2016 Kaikōura, New Zealand, earthquake: Preliminary seismological report. *Seismological Research Letters*, *88*(3), 727–739. https://doi.org/10.1785/0220170018

Kaneko, Y., & Fialko, Y. (2011). Shallow slip deficit due to large strike-slip earthquakes in dynamic rupture simulations with elasto-plastic off-fault response. *Geophysical Journal International*, *186*(3), 1389–1403. https://doi.org/10.1111/j.1365-246X.2011.05117.x

Kaneko, Y., Fukuyama, E., & Hamling, I. J. (2017). Slip-weakening distance and energy budget inferred from near-fault ground deformation during the 2016 Mw7.8 Kaikōura earthquake. *Geophysical Research Letters*, *44*, 4765–4773. https://doi.org/10.1002/2017GL073681

Kiser, E., & Ishii, M. (2017). Back-projection imaging of earthquakes. *Annual Review of Earth and Planetary Sciences*, *45*(1), 271–299. https://doi.org/10.1146/annurev-earth-063016-015801

Langridge, R. M., Ries, W. F., Litchfield, N. J., Villamor, P., Van Dissen, R. J., Rattenbury, M. S., et al. (2016). The New Zealand active faults database. *New Zealand Journal of Geology and Geophysics*, *59*, 86–96. https://doi.org/10.1080/00288306.2015.1112818

Lin, J., & Stein, R. S. (2004). Stress triggering in thrust and subduction earthquakes and stress interaction between the southern San Andreas and nearby thrust and strike-slip faults. *Journal of Geophysical Research*, *109*, B02303. https://doi.org/10.1029/2003JB002607

Litchfield, N. J., Van Dissen, R., Sutherland, R., Barnes, P. M., Cox, S. C., Norris, R., et al. (2014). A model of active faulting in New Zealand. *New Zealand Journal of Geology and Geophysics*, *57*(1), 32–56. https://doi.org/10.1080/00288306.2013.854256

Litchfield, N. J., *et al.* (2016). 14th November 2016 M 7.8 Kaikoura earthquake. Preliminary surface fault displacement measurements, version 2. *GNS Science*.

Mason, D. P., & Little, T. A. (2006). Refined slip distribution and moment magnitude of the 1848 Marlborough earthquake, Awatere Fault, New Zealand. *New Zealand Journal of Geology and Geophysics*, *49*(3), 375–382. https://doi.org/10.1080/00288306.2006.9515174

Meng, L., Inbal, A., & Ampuero, J. P. (2011). A window into the complexity of the dynamic rupture of the 2011 M_w 9 Tohoku-Oki earthquake. *Geophysical Research Letters*, *38*, L00G07. https://doi.org/10.1029/2011GL048118

Meng, L., Ampuero, J. P., Stock, J., Duputel, Z., Luo, Y., & Tsai, V. C. (2012). Earthquake in a maze: Compressional rupture branching during the 2012 M_w 8.6 Sumatra earthquake. *Science*, *337*(6095), 724–726. https://doi.org/10.1126/science.1224030

Meng, L., Ampuero, J. P., Luo, Y., Wu, W., & Ni, S. (2012). Mitigating artifacts in back-projection source imaging with implications for frequency-dependent properties of the Tohoku-Oki earthquake. *Earth, Planets and Space*, *64*(12), 1101–1109. https://doi.org/10.5047/eps.2012.05.010

Meng, L., Zhang, A., & Yagi, Y. (2016). Improving back projection imaging with a novel physics-based aftershock calibration approach: A case study of the 2015 Gorkha earthquake. *Geophysical Research Letters*, *43*, 628–636. https://doi.org/10.1002/2015GL067034

Michel, R., Avouac, J. P., & Taboury, J. (1999). Measuring ground displacements from SAR amplitude images: Application to the Landers earthquake. *Geophysical Research Letters*, *26*(7), 875–878. https://doi.org/10.1029/1999GL900138

Noda, H., Lapusta, N., & Kanamori, H. (2013). Comparison of average stress drop measures for ruptures with heterogeneous stress change and implications for earthquake physics. *Geophysical Journal International*, *193*(3), 1691–1712. https://doi.org/10.1093/gji/ggt074

Okada, Y. (1985). Surface deformation due to shear and tensile faults in a half-space. *Bulletin of the Seismological Society of America*, *75*, 1135–1154.

Poliakov, A. N., Dmowska, R., & Rice, J. R. (2002). Dynamic shear rupture interactions with fault bends and off-axis secondary faulting. *Journal of Geophysical Research*, *107*(B11), 2295. https://doi.org/10.1029/2001JB000572

Sieh, K., Jones, L., Hauksson, E., Hudnut, K., Eberhart-Phillips, D., Heaton, T., et al. (1993). Near-field investigations of the Landers earthquake sequence, April to July 1992. *Science*, *260*(5105), 171–176. https://doi.org/10.1126/science.260.5105.171

Townend, J., Sherburn, S., Arnold, R., Boese, C., & Woods, L. (2012). Three-dimensional variations in present-day tectonic stress along the Australia–Pacific plate boundary in New Zealand. *Earth and Planetary Science Letters*, *353*, 47–59.

Van Dissen, R., & Yeats, R. S. (1991). Hope fault, Jordan thrust, and uplift of the seaward Kaikoura Range, New Zealand. *Geology*, *19*, 393–396.

Wallace, L. M., & Beavan, J. (2010). Diverse slow slip behavior at the Hikurangi subduction margin, New Zealand. *Journal of Geophysical Research*, *115*, B12402. https://doi.org/10.1029/2010JB007717

Wallace, L. M., Kaneko, Y., Hreinsdóttir, S., Hamling, I., Peng, Z., Bartlow, N., et al. (2017). Large-scale dynamic triggering of shallow slow slip enhanced by overlying sedimentary wedge. *Nature Geoscience*, *10*(10), 765–770. https://doi.org/10.1038/ngeo3021

Wang, T., Wei, S., Shi, X., Qiu, Q., Li, L., Peng, D., et al. (2018). The 2016 Kaikōura earthquake: Simultaneous rupture of the subduction interface and overlying faults. *Earth and Planetary Science Letters*, *482*, 44–51.

Williams, C. A., Eberhart-Phillips, D., Bannister, S., Barker, D. H. N., Henrys, S., Reyners, M., & Sutherland, R. (2013). Revised interface geometry for the Hikurangi Subduction Zone, New Zealand. *Seismological Research Letters*, *84*, 1066–1073.

Witze, A. (2017). Ripple effects of New Zealand earthquake continue to this day. *Nature*, *544*(7651), 402–403. https://doi.org/10.1038/nature.2017.21876

Xu, W., Bürgmann, R., & Li, Z. (2016). An improved geodetic source model for the 1999 M_w 6.3 Chamoli earthquake, India. *Geophysical Journal International*, *205*(1), 236–242. https://doi.org/10.1093/gji/ggw016

Xu, X., Tong, X., Sandwell, D. T., Milliner, C. W. D., Dolan, J. F., Hollingsworth, J., et al. (2016). Refining the shallow slip deficit. *Geophysical Journal International*, *204*, 1867–1886.

Zhang, H., Koper, K. D., Pankow, K., & Ge, Z. (2017). Imaging the 2016 M_w 7.8 Kaikoura, New Zealand, earthquake with teleseismic P waves: A cascading rupture across multiple faults. *Geophysical Research Letters*, *44*, 4790–4798. https://doi.org/10.1002/2017GL073461

Zheng, A., Wang, M. F., Yu, X. W., & Zhang, W. B. (2018). Source rupture process of the 2016 Kaikoura, New Zealand earthquake estimated from the kinematic waveform inversion of strong-motion data. *Geophysical Journal International*, *212*(3), 1736–1746. https://doi.org/10.1093/gji/ggx505